Physics-based Modeling and Micro-burr Removal Mechanism Analysis for Laser-induced Plasma Deburring

Hanyu Song and Benxin Wu*

School of Mechanical Engineering, Purdue University, 585 Purdue Mall, West Lafayette, IN 47907, USA

Abstract: Burrs are often generated in manufacturing processes such as machining, and they often need to be removed. Micro deburring is often very challenging due to the large size ratios of burrs to their attached useful micro features and/or the fragility of the features, etc. The corresponding author's previous paper (Journal of Manufacturing Science and Engineering, 136(2): 024501) reports preliminary experimental study of a novel laser-induced plasma deburring (LPD) process, which has several potential advantages and could help address the challenges in micro deburring. However, the burr removal mechanism in the previous LPD experiment still requires further study to understand. In this paper, a physics-based model is developed for laser-induced plasma flow and plasma-burr interactions. The model is validated by comparing its predictions with some previous experimental measurements. Then the model is used to reveal the dominant burr removal mechanism in the aforementioned previous LPD experiment. Under the conditions studied, it has been found that the plasma-induced thermal effect on the burr is unlikely to play a major role in the burr removal. Instead, the high pressure induced by the plasma on the burr can induce stresses potentially large enough to remove the burr. Therefore, the burr removal is likely mainly through a mechanical mechanism instead of a thermal mechanism during the LPD process under the conditions studied.

Keywords: laser-induced plasma; deburring; micromachining

1. Introduction

There are numerous needs for micro devices, parts or structures in important fields, such as optics, electronics, biomedical, aerospace and automobile industries [1-5]. However, micro-manufacturing processes, such as micromachining, often produce microscale burrs that are attached to useful micro features of the workpiece, and the burrs are typically undesirable and need to be removed by a deburring process [6-13]. The time consumed and the cost induced by a

* Corresponding author: Benxin Wu, Associate Professor, School of Mechanical Engineering, Purdue University, 585 Purdue Mall, West Lafayette, IN 47907, USA, email: wu65@purdue.edu

deburring process could even exceed that by a micromachining process itself that produces the burrs [10].

The process of removing microscale burrs from microscale useful features of a workpiece is called micro deburring in this paper, which faces several challenges. For example, the size ratio of the burr over the useful feature that it is attached to is often larger than that for macro deburring [8]. The feature may often be fragile, while its surface quality and/or geometrical precision may have to satisfy high requirements. A complete removal of burrs without harming the feature to which they are attached can be challenging. The various sizes, shapes and/or locations of different burrs may require cumbersome re-alignments of the deburring tool and/or adjustments of the process parameters for some existing deburring technologies [8, 12, 13].

In the corresponding author's previous paper [14], a novel laser-induced plasma deburring (LPD) process is proposed and a preliminary experimental study is presented. LPD demonstrates a great potential to address the challenges in micro deburring. In LPD, laser-induced plasma plume is utilized to impact and remove various burrs in its expansion path (potentially without the need for cumbersome tool re-alignment and/or parameter readjustment for individual burr(s)). The plasma plume can naturally conform to the workpiece surface geometry. LPD does not have mechanical cutting tool wear problem. It can potentially work for both conductive and non-conductive materials.

Under the conditions studied in [14], it has been found that LPD can remove micro burrs without obvious size or shape change of the attached workpiece useful features observed in the microscopic images taken. In LPD, the plasma plume can be potentially generated by laser ablation of a portion of the workpiece, an auxiliary plate that is not a portion of the workpiece, and/or laser-induced breakdown of the ambient gaseous environment, etc. Laser-induced plasma deburring is

different from direct laser deburring [12, 13], where a burr is removed by direct laser irradiation onto the burr. In direct laser deburring, to remove a burr without harming the workpiece useful feature, it is often required that the laser beam is precisely aligned to irradiate around the burr with a suitable amount of energy depending on the burr size. Therefore, removing multiple micro burrs with different sizes, shapes and/or locations could often require very careful and cumbersome beam re-alignments and/or laser parameter adjustments. LPD can potentially avoid this disadvantage as introduced earlier.

However, despite the previous study in Ref. [14], lots of further work is still needed to gain a good fundamental understanding of the burr removal mechanism in LPD, which is important for its practical applications. It is proposed in Ref. [14] that the burr removal through one, or a combination, of the following two mechanisms might be possible: (1) thermal mechanism: the burr is removed due to plasma-induced thermal effect such as high temperature, melting and/or even vaporization, etc., and (2) mechanical mechanism, the burr is removed due to stresses generated by the pressures induced by the plasma onto the burr. However, the exact burr removal mechanism still requires further study to understand.

To better understand the burr removal mechanism in LPD, in this paper a physics-based model is developed to simulate the interaction between laser-induced plasma and a burr. First, the developed model will be validated by comparing its predictions with the time-resolved plasma images obtained from the experiments reported in the corresponding author's previous papers. Then, the validated model will be used to study laser-induced plasma flow around a burr, the plasma-induced heat transfer to and mechanical impact on the burr, and the temperature change of the burr. Finally, based on the model simulations, the fundamental burr removal mechanism will be analyzed for the LPD experiment reported in the corresponding author's previous paper [14].

2. The Model

Figure 1 shows the schematic diagram of the model setup, including the major governing equations solved in different sub-domains of the model. The model in this paper simulates the laser-induced plasma generation and evolution in an approach similar to that in the corresponding author's previous papers for plasma due to laser-induced surface vaporization from a solid (e.g., [15, 16]). However, please note that none of the authors' previous papers numerically modeled or simulated laser-induced plasma-burr interaction, which is the focus of this current paper and this paper's major novelty in comparison with the authors' previous papers.

The target material is a pure titanium. A laser beam (with ~200 ns full laser pulse duration) propagates downwards (in the –z direction) and irradiates the bottom of the microhole. The laser beam heats and melts a surface layer of the hole bottom wall. At a sufficiently high laser intensity, the melted surface temperature can well exceed the material melting point, causing significant vaporization from the surface and a plasma plume expanding upwards. The plasma will then impact the burr at the hole sidewall. Due to the surface vaporization and the associated material removal, the hole bottom wall surface will recede in the –z direction at a very small velocity of u_{vap}. In a coordinate system with its original point being fixed at the bottom wall surface, the heat transfer in the bottom wall condensed phase domain below z = 0 is governed by the following heat transfer equation [15-20]:

$$\rho_c \frac{\partial H}{\partial t} + \rho_c u_{vap} \frac{\partial H}{\partial z} = \frac{\partial}{\partial z}\left(k_c \frac{\partial T}{\partial z}\right) + \frac{1}{r}\frac{\partial}{\partial r}\left(r k_c \frac{\partial T}{\partial r}\right) + \frac{\partial I(r,z,t)}{\partial z} \qquad (1a)$$

where t is time, r and z are spatial coordinates, ρ_c and k_c are the condensed phase density and thermal conductivity, respectively, H is the material enthalpy, T represents temperature, and I is laser beam intensity that can be obtained by solving the following equation [15]:

$$\frac{\partial I(r,z,t)}{\partial z} = \alpha_c I \qquad (1b)$$

where α_c is the optical absorption coefficient of the condensed phase. Eq.(1b) can be solved based on the boundary condition at z = 0, which is: $I(r,0,t) = (1-R)I_0(r,t)$, where R is the optical surface reflectivity of the bottom wall condensed phase and $I_0(r,t)$ is the laser beam intensity reaching the bottom wall condensed phase surface. The relation between H and T can be constructed based on the titanium solid and liquid specific heat capacities and latent heat of melting. In constructing the relation, it has been assumed that melting starts at $T_m - 0.5\ K$ and finishes at $T_m + 0.5\ K$, where T_m is the melting point.

The evolution of the temperature, density as well as velocity of the target (Ti) vapor and the ambient air inside the microhole can be simulated by solving the two-dimensional axisymmetric compressible gas dynamic equations [15, 16, 20-23]:

$$\frac{\partial \rho_v}{\partial t} + \frac{\partial(\rho_v V_r)}{\partial r} + \frac{1}{r}(\rho_v V_r) + \frac{\partial(\rho_v V_z)}{\partial z} = 0 \qquad (2a)$$

$$\frac{\partial \rho_a}{\partial t} + \frac{\partial(\rho_a V_r)}{\partial r} + \frac{1}{r}(\rho_a V_r) + \frac{\partial(\rho_a V_z)}{\partial z} = 0 \qquad (2b)$$

$$\frac{\partial \rho V_r}{\partial t} + \frac{\partial \rho V_r^2}{\partial r} + \frac{1}{r}(\rho V_r^2) + \frac{\partial(\rho V_r V_z)}{\partial z} = -\frac{\partial P}{\partial r} \qquad (2c)$$

$$\frac{\partial \rho V_z}{\partial t} + \frac{\partial \rho V_r V_z}{\partial r} + \frac{1}{r}(\rho V_r V_z) + \frac{\partial(\rho V_z^2)}{\partial z} = -\frac{\partial P}{\partial z} \qquad (2d)$$

$$\frac{\partial(0.5\rho V^2 + E_i)}{\partial t} + \frac{\partial[(0.5\rho V^2 + E_i + P)V_r]}{\partial r} + \frac{1}{r}(0.5\rho V^2 + E_i + P)V_r + \frac{\partial[(0.5\rho V^2 + E_i + P)V_z]}{\partial z} = \alpha I + \frac{\partial}{\partial z}\left(k_g \frac{\partial T}{\partial z}\right) + \frac{1}{r}\frac{\partial}{\partial r}\left(r k_g \frac{\partial T}{\partial r}\right) \qquad (2e)$$

where ρ_v and ρ_a are the density of the target vapor and the ambient air, respectively, $\rho\ (= \rho_v + \rho_a)$ is the total density, P denotes the pressure, V_r, V_z and V are the r-direction, z-direction and total

velocities, respectively, E_i is the internal energy per unit volume, I is the laser beam intensity, α and k_g is the optical absorption coefficient and the thermal conductivity of the gaseous phase, respectively, and T is the temperature.

The target vapor atoms leaving the melted condensed phase surface are initially not in an equilibrium velocity distribution, and they will reach an equilibrium distribution after passing a thin layer right above the melt surface, called Knudsen layer (whose thickness can be neglected in this model) [15, 17, 18, 20, 24-27]. The relations between the melt surface temperature at the bottom of the Knudsen layer and the vapor parameters at the top of the Knudsen layer can be called "Knudsen layer relations" and are available in the literature. The gas dynamic equations (Eq.2) and the aforementioned heat transfer equation (Eq.1a) are related with each other via the following Knudsen layer relations [15, 17, 18, 20, 24-27]:

$$\frac{T_v}{T_{c,s}} = \left[\sqrt{\pi\left(\frac{\beta(\gamma-1)}{2(\gamma+1)}\right)^2 + 1} - \sqrt{\pi}\frac{\beta(\gamma-1)}{2(\gamma+1)}\right]^2 \tag{3a}$$

$$\frac{\rho_v}{\rho_{c,s}} = \sqrt{\frac{T_{c,s}}{T_v}}\left[(\beta^2+0.5)\exp(\beta^2)erfc(\beta) - \frac{\beta}{\sqrt{\pi}}\right] + 0.5\frac{T_{c,s}}{T_v}\left[1-\sqrt{\pi}\beta\exp(\beta^2)erfc(\beta)\right] \tag{3b}$$

$$M = \frac{V_v}{C_s} = \frac{V_v}{\sqrt{k_b T_v \gamma/m}} = \begin{cases} \frac{\left(\frac{P_{c,s}}{P_v}\right)^{\delta}-1}{1-\Phi^{\delta}}, & \text{if } \left(\frac{P_{c,s}}{P_v}\right) < 1 \ (condensation) \\ \frac{1-\left(\frac{P_v}{P_{c,s}}\right)^{d}}{1-\mathrm{A}^{d}}, & otherwise \ \ (vaporization) \end{cases} \tag{3c}$$

$$\rho_c u_{vap} = \rho_v V_v \tag{3d}$$

where T_v and $T_{c,s}$ are the temperatures on the vapor side and the condensed phase side of the Knudsen laser (KL), respectively (i.e., $T_{c,s}$ is the condensed phase surface temperature), ρ_v is the vapor density right on the top of the KL, γ denotes specific heat ratio, k_b is the Boltzmann constant,

$\beta = M(0.5\gamma)^{0.5}$, M, V_v , P_v and C_s are the vapor Mach number, z-direction velocity, pressure and sound speed right above the KL, respectively, Φ and δ are parameters which are related to $ln(T_v/T_{c,s})$ as given in [17], A and d are constants taken from [17], m is the vapor atomic mass, and $\rho_{c,s}$ is the saturation vapor density at $T_{c,s}$, which is obtained based on the approximate assumption of ideal gas and the saturation vapor pressure, $P_{c,s}$, calculated by the Clausius-Clapeyron equation [27]:

$$P_{c,s}(T_{c,s}) = P_0 e^{[\frac{Hev}{Rg T_0}(1-\frac{T_0}{T_{c,s}})]} \quad (4)$$

where P_0 is saturation vapor pressure at the temperature of T_0, R_g is the specific gas constant, and H_{ev} is the vaporization latent heat.

From the Knudsen layer relations, it can be seen that gas dynamic processes right above the Knudsen layer attached to the condensed phase surface strongly affect the surface vaporization or condensation process. If the vapor pressure right above the Knudsen layer, P_v, is smaller than the vapor saturation pressure corresponding to the condensed phase surface temperature, $P_{c,s}$, then the vaporization process occurs. If the former is larger than the latter, then vapor condensation occurs and the vaporized material will come back to the melt surface. In the model, the energy loss or gain for the condensed phase surface due to the vaporization or condensation process is considered.

In order for the gas dynamic equations to be solvable, the gaseous phase equation of state (EOS) is needed. It has been found that under the conditions simulated, the air temperatures are typically low, and high-temperature air regions, if any, are typically very thin. Hence, for air, the ideal gas EOS is applied without considering ionization. The air internal energy E_i and pressure P

are assumed to be related to its temperature (T) and molecular number density (n_{air}) by: $E_i = \frac{5}{2} k_b T n_{air}$ and $P = k_b T n_{air}$ [28].

For the high temperature vapor that could be ionized and has free electrons, the procedure introduced next will be used to obtain its EOS, which can tell the vapor pressure and internal energy at each given pair of vapor temperature and density in the temperature and density ranges involved in the model simulations.

The vapor free electron number density is governed by the Saha equation [28, 29]:

$$\frac{n_e n_{i+1}}{n_i} = 2 \frac{w_{i+1}}{w_i} \left[\frac{2\pi m_e k_b T}{h^2}\right]^{1.5} e^{-\frac{\theta_i}{k_b T}} \qquad (5)$$

where n_e is the free electron number density, n_i and n_{i+1}denotes the number density of i-fold and (i+1)-fold ionized atoms, respectively, whose partition functions are w_i and w_{i+1}, respectively (which can be approximately replaced by the ground state statistical weights in the equation), m_e is the electron mass, h is Planck's constant, θ_i is the ionization potential for the *i* to *i+1* ionization process. When i = 0, n_i denotes the neutral atom number density. The free electron number density and the number densities of ionized atoms also satisfy the following relation [29]:

$$n_e = \sum_{i=1}^{i_{max}} i n_i \qquad (6)$$

where i_{max} is the largest charge number of ions considered in the calculation. The vapor mass density ρ_v and the total number density of heavy particles n_p (ions and neutral atoms) are related by:

$$\rho_v = m_a n_p = m_a \sum_{i=0}^{i_{max}} n_i \qquad (7)$$

where m_a is the atomic mass for the vapor. For the calculations in this paper, i_{max} is chosen to be 5. Hence, five Saha equations in the form of Eq.5 (where i = 0, 1, ..4), together with Eqs.6 and 7, are solved for each given temperature-density pair, (T, ρ_v), following a solution procedure as

introduced in [29]. In this way, the number densities of free electrons, neutral atoms and ions can be calculated. Then the vapor internal energy E_i and pressure P at the given temperature and density can be obtained by [28, 29]:

$$P = k_b T(n_e + n_p) \tag{8}$$

$$E_i = 1.5k_b T\left(n_e + n_p\right) + \sum_{i=1}^{i_{max}}(n_i \sum_{j=0}^{i-1}\theta_j) \tag{9}$$

For the thermal conductivity of the air, a constant value under the typical room condition (300 K and 0.1 MPa) determined based on [30] is used. This approximate simplification is expected to be reasonable, because under the conditions simulated it has been found that air temperatures are typically low and high-temperature air regions, if any, are typically very thin. It has been found that the laser-induced target vapor can be in a partially ionized state under the conditions simulated. For the vapor, the thermal conductivity due to free electrons is used, which can be calculated by [31]:

$$k_e = k_b n_e \sqrt{\frac{8k_b T}{\pi m_e}} \frac{1}{(2+\sqrt{2})n_e Q_{ei} + 2n_0 Q_{en}} \tag{10}$$

where Q_{ei} and Q_{en} are the electron-ion and electron-neutral atom collision cross sections, respectively. In the simulations in this paper, the effect of the Q_{en} term has been neglected, while Q_{ei} is given by [31]:

$$Q_{ei} = 6\pi \left(\frac{Ze^2}{12\pi\varepsilon_0 k_b T}\right)^2 ln\left(\frac{12\pi}{Ze^3}\sqrt{\frac{\varepsilon_0^3 k_b^3 T^3}{n_e}}\right) \tag{11}$$

where Z is the ionic charge number, ε_0 is the permittivity of vacuum and e is the electron charge. Eq.(10), written in its current form, has the underlying assumption that the number density of free electrons is the same as that for all the ions. This assumption is reasonable under the conditions

investigated in this paper, where the simulation results show that 1-fold ionized vapor atoms dominate over other types of ions. For the calculation with Eq.(11) (as well as that for Eq.(12) given later), only the 1-fold ionized atoms are considered.

The optical absorption coefficient of the vapor plasma region due to the electron-ion inverse bremsstrahlung (IB) effect is given by [32]:

$$\alpha = \left(1 - e^{-\frac{h\nu}{k_b T}}\right) \frac{4}{3} \sqrt{\frac{2\pi}{3k_b T}} \frac{n_e n_i Z^2}{hcm_e^{1.5} \nu^3} \frac{e^6}{(4\pi\varepsilon_0)^3} \qquad (12)$$

where c is the speed of light in vacuum, n_i is the ion number density, ν is the frequency of the laser light, and e is electron charge. Under the conditions simulated in this paper, if laser energy absorption by plasma is not considered, the model can still predict the vapor plasma temperatures as well as electron number densities, etc., and based upon these the optical absorption coefficient can be calculated using Eq.(12). Based on the calculated absorption coefficient values, it is expected that neglecting the optical absorption of laser energy by plasma should not greatly influence the model calculation results to the extent of hurting the main propose of this paper, which is to qualitatively reveal the dominant burr removal mechanism in LPD for the studied condition. Hence, the absorption coefficient has been approximately neglected in the model calculations in this paper. It has also been found that the vapor ionization degree is small (n_e/n_p is typically less than 0.15). Hence, the effect of free electrons is neglected for Eqs.3 and 4. As introduced earlier, free electrons are considered when constructing the vapor EOS to solve Eq.2.

For the microhole sidewall and the burr region, the 2D axisymmetric heat conduction equation is solved (but without the advection term as in Eq.1a). For the top and bottom burr-gaseous phase interfaces, the following boundary condition is applied:

$$-k_c \frac{\partial T}{\partial z}_{(condensed\ phase\ side)} = -k_g \frac{\partial T}{\partial z}_{(gaseous\ phase\ side)} \quad (13)$$

For the burr side surface, the boundary condition is:

$$-k_c \frac{\partial T}{\partial r}_{(condensed\ phase\ side)} = -k_g \frac{\partial T}{\partial r}_{(gaseous\ phase\ side)} \quad (14)$$

For the microhole sidewall region, a boundary condition similar to that for the burr side surface is applied at the sidewall surface. The domain sizes of the hole bottom wall and sidewall are chosen to be sufficiently large such that at their boundaries not facing the gaseous phase in the microhole, the original room temperature (300 K) can be assumed.

For each of the microhole bottom wall surface, sidewall surface and the burr surfaces, the no-slip boundary conditions is applied, except that for the hole bottom wall surface, the boundary condition for V_z is based on the Knudsen layer relations introduced earlier.

The thermal radiation between the workpiece condensed phase surfaces (including the microhole sidewall and the burr surfaces) and the gaseous phase as well as that within the gaseous phase are expected to be not critical, and are neglected in the model. When solving the heat transfer equation for the microhole bottom wall condensed phase domain (i.e., Eq.1a), a boundary condition is applied at the bottom wall surface, where the z direction heat conduction and enthalpy advection flux in the condensed phase towards the surface should be equal to the sum of the latent heat consumption due to vaporization, the advection flux of the vapor internal and kinetic energy, the work done by the gaseous phase pressure, and the net surface thermal radiation flux. When vapor condensation occurs, a boundary condition based on a similar concept can also be applied. For the studied conditions, the thermal radiation flux is expected to be not critical and hence is very approximately calculated as blackbody radiation between the bottom wall surface and an

ambient environment at the initial temperature. At t = 0, the temperature of all the solid regions is assumed to be 300 K, while the ambient air is assumed to be at 300 K and 0.101 MPa.

The governing equations in the hole bottom condensed phase region, the gaseous phase region inside the hole, and the hole sidewall and burr region are solved numerically using a finite difference explicit method based on an in-house developed code. Locally more refined meshes are used in the near-surface region of the hole bottom wall and sidewall. Besides, in the burr region near its interface with the gaseous phase, very small mesh sizes (along the direction normal to the interface) are used to resolve the possible high temperature gradient in the normal direction. The gas dynamic equations in the microhole are solved with the essentially non-oscillatory (ENO) scheme from [33]. The governing equations in the hole bottom condensed phase region and the gaseous phase region are related through the Knudsen layer relations (Eq.3). At each numerical time step, they are solved together following a procedure similar to that in the corresponding author's previous paper [15], where more details can be found. At each time step, after the gaseous phase equations are solved and the gaseous phase temperature field is obtained, the heat transfer equation in the burr region can be solved with a finite difference method [22] based on the boundary conditions given in Eqs.13 and 14. The heat transfer equation governing the temperature evolution of the hole sidewall region is numerically solved similarly. Therefore, the model can predict the distribution in space and the change with time for the temperature, density, pressure and velocity of the gaseous phase located inside the microhole, as well as the temperature of the burr, the hole sidewall and bottom wall regions.

Table 1 shows some major material properties for titanium used in the model [34-37]. For the titanium thermal conductivity, density and specific heat, a constant value each is used for the solid phase and a different constant value each is used for the liquid phase. Based on the

information in [36], the solid titanium complex index of refraction, n_r+in_i, at 1064 nm is determined. Based on this, the solid titanium surface reflectivity and optical absorption coefficient are calculated using the Fresnel equations and the relation, $\alpha = 4\pi n_i/\lambda$ (where λ is the laser wavelength), respectively [38]. The calculated reflectivity and optical absorption coefficient are used for both the solid and the melted titanium in this model for the bottom wall domain, because their reliable values for melted titanium at 1064 nm have not been found by the authors in the literature.

As shown later, despite the approximations in the model, the model-experiment agreements are reasonably good for the situations studied, which should be sufficient for the purpose of this paper, which is to *qualitatively* reveal the dominant burr removal mechanism for the LPD experiment reported in the corresponding author's previous paper [14]. Certainly, obvious room still exists for further improvement of the model.

3. Results and Discussions

Section 3.1 will present the validation of the developed model by comparing its predictions with the experimental measurements from the corresponding author's previous papers [14, 39]. Section 3.2 will introduce and discuss the model-predicted results on laser-induced plasma flow in a microhole with a burr on its sidewall, the plasma-induced pressure onto the burr surface, and the burr temperature change due to the plasma-induced heat transfer. Based on the model calculations, Section 3.3 will analyze the burr removal mechanism for the laser-induced plasma deburring experiment reported in the corresponding author's previous paper [14].

3.1 Experimental Validation of the Model

Figure 2 shows the model-predicted gaseous phase temperature contour plots versus the intensified CCD (ICCD) camera images at different moments for plasma plume induced by ~200-ns laser pulse ablation of a flat titanium target without any sidewall confinement (for both the modeled and the experimental conditions). The ICCD images are taken from the corresponding author's previous paper [39]. It can be seen from Fig.2 that the top front locations relative to the titanium target surface for the high-temperature region in the gaseous phase obtained via the model simulation have a reasonably good agreement with the plume top front locations in the ICCD images. The plasma plume front expansion speed is strongly affected by the plasma pressure, which then depends on its temperature and density (via the plasma equation of state). Hence, the plume top front location agreement also serves as an indirect test of the model predicted plasma pressure (and hence temperature and density). Fig.2 shows that the shapes of the model-predicted high-temperature gaseous phase regions also agree reasonable well with plasma plume shapes in the ICCD images. Hence, overall Fig.2 has demonstrated a reasonably good model-experiment agreement for the plasma induced by laser ablation of a flat titanium target without any sidewall confinement. In the model simulation for Fig.2 (as well as those for Figs.3 to 8), the laser beam intensity is assumed to follow a Gaussian distribution and the laser pulse shape is similar to that given in Fig.1b of Ref.[39].

Figure 3 shows another comparison between the model prediction (Fig.3a) and the ICCD imaging result (Fig.3b) for laser-induced plasma plume. In the corresponding author's previous paper [14], in-situ time-resolved images were captured using an ICCD camera for the plasma plumes in titanium micro-channels induced by laser ablation of the channel bottom, where the laser has a full pulse duration of ~200 ns, a wavelength of ~1064 nm, a pulse energy of ~0.4 mJ, and a diameter of ~30 μm (near the channel bottom). The channel has two sidewalls and the other two

sides are open. Figure 3b shows the transient ICCD image of the plasma plume at t = 100 ns (where t = 0 is defined as the moment when the laser pulse starts) in a ~110 μm wide channel taken from Ref. [14] (where more experiment-related details can be found). Figure 3a shows the gaseous phase temperature predicted by the model in this paper for plasma in a 110 μm-diameter microhole in a titanium target induced by laser ablation of the hole bottom (burr is not included in this simulation). In the model simulation, the assumed laser conditions are about the same as those in the experiment for Fig.3b. The incoming laser beam intensity is assumed to follow the Gaussian distribution, and the temporal shape of the laser pulse is assumed based on the measured one for the SPI G3.0 laser used in [14], and the pulse shape is similar to that shown in Fig.1b of [39]. It can be seen from Fig.3 that the gaseous phase high-temperature region top front location predicted by the model agrees reasonably well with the plasma top front location in the ICCD image (although the former is a little behind). The ICCD image shows two bright streaks in the plasma plume region near the sidewall, which are consistent with the model-predicted temperature field as indicated by the red arrows in the figure. The model simulation reveals that the two bright streaks observed in the ICCD image should be high-temperature regions formed due to the confinement effect of the sidewall on the plasma expansion in the lateral direction. In the ICCD image, a bright plume region exists above the two streaks. A corresponding high-temperature region is also shown in the model-predicted temperature contour plot (as indicated by the green arrows), but with a smaller size.

The model-experiment agreements shown in Figs.2 and 3 are reasonably good (although some differences do exist), considering the following factors: (1) The laser-induced plasma generation and evolution process is very complicated. (2) The model is a fully predictive model based on process conditions and material properties without any free adjustable or fitting variable. (3) The model involves high-temperature molten metal thermal and optical properties, for which

fully accurate and reliable values are difficult to find in the literature (if they exist at all). Such a challenge is difficult to completely overcome. Approximate assumptions have been made related to the material properties as described earlier in this paper. (4) For the plasma induced in the microchannel shown in Fig.3, in the experiment the channel bottom wall surface may not be fully flat or smooth, adding an additional uncertainty in the model-experiment comparison. Figure 3 also suggests that for the given situation the early-stage laser-induced plasma evolution in such a micro-channel is reasonably similar to that in a microhole whose diameter is equal to the channel width. The accuracy of the model is expected to be sufficient for the purpose of this paper, which is to qualitatively reveal the dominant burr removal mechanism in LPD under the studied condition.

3.2 Simulation Results and Discussions for Laser-induced Plasma Evolution in a Microhole and Plasma Interaction with a Burr on the Hole Sidewall

Next, the validated model will be applied to study the evolution of laser ablation-induced plasma in a microhole in a titanium target and the interaction of the plasma with a burr on the hole sidewall.

Figure 4 shows the model-predicted temperature and pressure contour plots for the gaseous phases inside the microhole with a 30×10 μm burr on its sidewall. The laser pulse has a full duration of 200 ns and starts ablating the hole bottom at t = 0, which generates a plasma plume (ionized vapor). Figure 4 shows at t = 30 ns, the plume high-temperature and high-pressure fronts have not reached the hole sidewall yet. By t = 50 ns, the plume lateral expansion has already felt the restriction of the microhole sidewall, which reflects the pressure wave from the plume. As a result, this generates a high-temperature/pressure zone near the sidewall as shown in the contour

plots in Fig.4 for t = 70 and 100 ns. At t = 120 ns, the plasma front has already passed the burr location. The burr partially blocks the plasma upwards expansion. Hence, high temperatures and pressures are developed in a small region below the burr as shown in the contour plots for t = 120 ns. The plume expands through the central opening formed by the burr. Then the pressure wave front propagates to and is then reflected by the sidewall again as shown in the contour plots for t = 170 ns.

Figure 5 shows the temperature and pressure contour plots for the gaseous phases in the region near the burr at t = 120 ns. It can be seen from the temperature contour plot that at t = 120 ns a high-temperature gaseous phase region exists near the burr bottom surface, where the gaseous phase peak temperature exceeds ~8000 K. The pressure contour plot shows a high pressure region below the burr bottom surface at t = 120 ns, where the pressures are typically on the order of tens of MPa. As mentioned earlier, it is expected that the formation of the high-temperature and high-pressure regions is due to the partial blocking of the plasma plume flow by the burr.

Figure 6a shows the model-predicted temperature distributions along the horizontal direction on the burr bottom surface at t = 100, 120, 150 and 170 ns, while Figure 6b shows the temperature distributions along the vertical direction on the burr side surface. It can be seen that although a high temperature zone may exist in the gaseous phase nearby as shown in Fig.5, the burr surface temperature is not very high. At t = 170 ns, the peak temperature on the burr bottom surface occurs at the lower right corner point of the burr, which is less than 1200 K and is still several hundred degrees lower than the titanium melting point [34]. Figure 6c shows the temperature distribution at t = 170 ns along the oblique direction that starts from the burr corner point and has an angle of 45^{o} relative to the horizontal direction as indicated by the green line in the schematic inserted. It can be seen that along this oblique direction, the temperature drops to

below 650 K within ~500 nm. Hence, the plasma-induced heat-affected layer in the burr is extremely thin.

The high temperature gradient in the burr surface layer shown in Fig.6c implies a high transient heat flux into the burr. However, due to the short, ~200-ns laser pulse duration (and hence the short high-temperature plasma lifetime that should be on a similar time scale as implied by the previous ICCD imaging study reported in the corresponding author's prior paper [39]), the total energy transferred into the burr per unit burr surface area should still be small and not able to greatly drive up the temperatures of a significant portion of the burr to remove it mainly via the thermal mechanism. It should be noted that most of the other portions of the burr bottom and right surfaces typically have much lower temperatures than the burr bottom-right corner, as implied by Fig.6a and b.

Although the plasma plume has high peak temperatures, its internal energy per unit volume and unit temperature is very low due to its significantly much smaller mass density than that for the burr condensed phase. Thus, as the plume front starts contacting the burr, even if a relatively small amount of energy is transferred from the plume into the burr, the plume temperature at the burr-plume interface (on the gaseous phase side) drops significantly. As a result, the interface temperatures can be much lower than those in the plasma high-temperature region nearby.

Figure 7 shows the model-predicted distributions of pressures exerted by the gaseous phase onto the bottom surface of the burr at t = 100, 110, 120 and 170 ns, as well as those for the top surface of the burr at different moments. For the burr bottom surface, at t = 100 ns, the pressure is at the initial value because the pressure wave front has not reached the burr yet. At t = 110 ns, a pressure peak exists near the 0 position (the burr-sidewall connection location). This is because the plasma-induced pressure wave front touches this region first. The pressure distribution

becomes more uniform at t = 120 ns and 170 ns. The peak pressure is ~28, ~20 and ~13.5 MPa at t = 110, 120 and 170 ns, respectively, for the burr bottom surface, while it is only a few MPa or less for the burr top surface at the moments given in the figure. It is expected that the large pressures exerted on the burr may induce significant stresses in the connection plane between the burr and the sidewall. This will be discussed in Section 3.3 of this paper.

Figure 8 shows the microhole sidewall surface temperature distributions along the vertical direction at t = 100, 120, 150 and 170 ns. It can be seen that despite the high peak temperature of the gaseous phase, the surface temperature of the microhole sidewall is quite low. At all the given moments, the peak temperature is less than 325 K. This implies that the plasma will unlikely cause any significant thermal damage to the microhole sidewall under the conditions studied.

In a short summary, under the conditions studied, Figs.4 to 8 show that although the laser-induced plasma has high peak temperatures during its early-stage evolution, the thermal transfer process from the gaseous phase to the burr is *not* able to greatly drive up the temperature of a significant portion of the burr. The plasma does not cause significant temperature rise for the microhole sidewall. On the other hand, the mechanical impact induced by the expanding plasma may cause high pressures onto the burr surface, which may induce significant mechanical stresses inside the burr.

3.3 Analysis of Burr Removal Mechanism in the Previous LPD Experiment based on the Model Simulations

The corresponding author's previous paper [14] reports LPD experiments on removing burrs from a micro-channel sidewall by plasma induced by laser ablation of the channel bottom for a titanium workpiece. The micro-channels are made using wire electrical discharge machining

(EDM), which have burrs on their sidewalls. Ref.[14] shows that LPD with ~200-ns duration and ~1064-nm wavelength laser pulses is able to effectively remove burrs from the sidewalls of the channel. More details related to the experiment can be found in Ref. [14]. In this section, the dominant burr removal mechanism in the previous LPD experiment in [14] will be revealed based on the simulation results of the model in this paper.

In one of the major experimental conditions in [14], the channel width (~110 μm) and depth are close to the microhole diameter (110 μm) and depth (370 μm), respectively, for the model simulation results in Figs.3 to 8 of this paper. In the experimental condition, the typical major laser parameters are also close to those in the simulation in this paper. The optical micrograph in [14] shows that burrs are on various locations of the channel sidewall with irregular shapes. Most of the burrs are located not very far away from the middle depth location of the sidewall. The burr sizes observed in the micrograph are typically on the scale of tens of microns. It is expected that the 30×10 μm burr at the middle depth location, as assumed in the model simulation in this paper, should have a sufficient similarity to help **qualitatively** reveal the dominant burr removal mechanism in the LPD experiment. In addition, as shown in the model-experiment comparison in Fig.3 of this paper, for the studied situation the early-stage expansion of plasma induced by laser ablation in a microhole is similar to that in a micro-channel when the laser conditions are similar and the hole diameter is close to the channel width. Therefore, it is expected that **the simulation results by the model in this paper can be used to reveal the dominant burr removal mechanism for the author's aforementioned previous LPD experiment** reported in Ref.[14] at least in the **qualitative or semi-quantitative** sense, which is sufficient for the purpose of this paper.

As shown in Fig.6 and discussed in Section 3.2, the model simulation shows that the plasma-induced heat transfer to the burr surface is not able to greatly drive up the temperature of a significant portion of the burr. At t = 170 ns, the burr surface peak temperature is still much lower than the titanium melting point and the temperature drops to below ~650 K within an extremely thin layer of ≤~500 nm near the burr surface. Hence, it is expected that the thermal mechanism (i.e., the burr temperature change due to plasma-induced heat transfer to the burr) does not play a major role in the burr removal in the aforementioned LPD experiment reported in the corresponding author's previous paper [14].

Therefore, the plasma-induced mechanical effect on the burr seems to be the major remaining possible mechanism for the burr removal. This will be further discussed next based on the model simulation results. As discussed earlier, for the studied situation, the early-stage plasma expansion in the microhole predicted by the model in this paper is reasonably similar to that in the micro-channel during the aforementioned LPD experiment in [14] when major laser parameters are similar. Hence, using the model-predicted pressures on the burr induced by the plasma, the typical stresses induced in the burrs during the aforementioned LPD experiment can be very approximately estimated.

The purpose of this paper is to qualitatively reveal the dominant burr removal mechanism for the LPD experiment. Hence, a rough and quick estimation of the scale of the stresses in the burr is sufficient. The burr on the micro-channel sidewall is approximately assumed to be a beam that is 30 μm long and 10 μm thick (i.e., in a geometry and location similar to the burr in Fig.4, except that the channel burr has a certain width *w* in the paper plane's normal direction, along which the spatial gradient of the plasma-induced pressure is neglected). Based on this approximate assumption, the stresses in the burr can be roughly estimated based on the simple elastic beam

theory as introduced in [40]. Although this quick and simple calculation can only give an estimation of the stresses in the semi-quantitative sense, it is sufficient for this paper's purpose of qualitatively revealing the dominant burr removal mechanism.

Figure 9a shows the estimated history of the normal stress for Point A (as defined in the schematic in Fig.1) of a 30×10 μm burr, which is located on the channel sidewall and whose center is 185 μm above the channel bottom (i.e., at the middle depth of the channel). The stress is zero until t = ~106 ns, when the plasma-induced pressure wave front reaches the burr. The magnitude of the stress increases and reaches a peak value of ~800 MPa at t = ~114 ns, after which the stress magnitude decreases. Hence, it can be seen that due to the plasma-induced pressures on the burr, very large tensile stresses can be generated in the burr in its connection plane with the channel sidewall. Figure.9b shows the history of the average shear stress for the entire burr-sidewall connection plane. Similar to the normal stress in Fig.9a, the shear stress in Fig.9b also starts increasing at t = ~106 ns, and then reaches the peak value of ~80 MPa at t = ~114 ns. The peak magnitude of the average shear stress is smaller than that for the normal stress.

Figure 9 also shows the stress histories for a 30×10 μm burr located 125 μm above the channel bottom. The peak magnitude of the tensile stress for Point A (as defined in the schematic in Fig.1) in the burr-sidewall connection plane is ~650 MPa, which is close to that for the burr located 185 μm above the channel bottom. In addition, Figure 9 shows the stress histories for a 30×15 μm burr located 185 μm above the channel bottom (i.e., at the middle depth of the channel). The burr has a large thickness-to-length ratio. Due to its larger thickness, the peak magnitude of the tensile stress for Point A in the burr-sidewall connection plane is smaller than that for the 30×10 μm burr at the same location, but the stress is still quite significant.

In a short summary, the results in Fig.9 suggest that very large peak tensile stresses can be induced in the burr-channel sidewall connection plane during the aforementioned previous LPD experiment in [14]. The peak tensile stress magnitudes shown in Fig.9a exceed or at least are reasonably close to the typical tensile strengths of a pure bulk titanium [41]. The strength at the burr-sidewall connection location could be obviously weaker than that for a bulk titanium. Hence, the large tensile stresses shown in Fig.9a can potentially break the burr away from the sidewall, particularly considering that multiple laser pulses are fired in the LPD experiment [14]. In other words, the results in this paper suggest that the burr removal should be mainly due to the mechanical effect, instead of the thermal effect, induced by the plasma on the burr during the aforementioned LPD experiment reported in the corresponding author's previous paper [14]. Although high pressures can also be induced onto the sidewall, due to its different geometrical shape from the burr, it is expected that the generated stresses in the sidewall are unlikely to damage the sidewall for the condition studied.

It should be noted that the burr removal mechanism could vary with the LPD process conditions (such as laser parameters) and material types, etc. Hence, it could be good future work to perform further studies under different conditions for a better understanding of the burr removal mechanism in LPD. The physics-based model developed in this paper for laser-induced plasma flow and plasma-burr interaction appears to be sufficient for the purpose of this study. On the other hand, there is certainly room to improve the model, which includes (but is not necessarily limited to) the accuracy improvement of the material properties used. In this paper, the laser-induced plasma generation is modeled based on the assumption of vaporization from the condensed phase surface of the bottom wall. The model-predicted condensed phase surface temperature under the

conditions studied is much lower than the thermodynamic critical temperature of titanium [42]. Hence, the surface vaporization assumption should be valid.

4. Conclusions

The corresponding author's previous paper [14] reports preliminary experimental study of a novel laser-induced plasma deburring (LPD) process, which has several potential advantages that could help address the challenges in micro deburring. However, the burr removal mechanism in the previous LPD experiment still requires further study to understand.

Due to very small spatial and time scales involved, it is very challenging to directly measure the plasma plume-induced pressures on the burr, or the time-resolved spatial distributions of temperatures in the burr and the plume near their interface. Hence, in this paper, a physics-based model is developed for laser-induced plasma flow and plasma-burr interaction. The model is validated by comparing its predictions with the previous experimental measurements. The plasma plume front expansion speed is strongly affected by the plasma pressure, which then depends on its temperature and density (via the plasma equation of state). Hence, the plume top front location agreements shown in Figs. 2 and 3 also serve as an indirect test of the model predicted plasma pressure (and hence temperature and density).

Under the conditions studied, it has been found that the plasma-induced heat transfer to the burr is not sufficient to greatly drive up the temperature of a significant portion of the burr. Hence, the plasma-induced thermal effect on the burr is unlikely to play a major role in the burr removal during LPD in the studied situation (although the possibility of a minor role still exists). On the other hand, the model simulations show that high pressures can be induced by the plasma on the burr surface, which can lead to very large tensile stresses in the burr-sidewall connection plane.

The magnitude of the stresses can be potentially sufficient to break the burr from the sidewall to which it is attached. Therefore, the plasma-induced mechanical effect on the burr is likely to play a major role in the burr removal during LPD in the situation studied.

The difficulty to remove a burr could depend on the burr size and/or shape. The burr removal mechanism in LPD may be affected by the plasma conditions, which then depend on laser parameters. LPD is still in a relatively early stage of its development. Lots of further work is still needed to understand the performance and burr removal mechanism of LPD under various conditions.

Acknowledgment

This material is based upon work supported by the National Science Foundation under Grant No. CMMI 1911361. The awardee university for this grant is Purdue University (West Lafayette, IN).

List of References

1. Ehmann, K.F., 2007. A synopsis of U.S. micro-manufacturing research and development activities and trends. Proceeding of 4M2007 Conference on Multi-Material Micro Manufacture, 2007.
2. Janson, S. W., Helvajian, H., and Breuer, K., 1999. MEMS, microengineering and aerospace systems. 30th Fluid Dynamics Conference, p. 3802.
3. Dario, P., Carrozza, M.C., Benvenuto, A., and Menciassi, A., 2000. Micro-systems in biomedical applications. J. Micromech. Microeng., 10(2): 235-244.
4. Ashraf, M.W., Tayyaba, S., and Afzulpurkar, N., 2011. Micro electromechanical systems (MEMS) based microfluidic devices for biomedical applications. Int. J. Mol. Sci., 12(6): 3648-3704.
5. Masuzawa, T., 2000. State of the art of micromachining. CIRP Annals – Manufacturing Technology, 49(2): 473-488.
6. Gillespie, L.K., 1979. Deburring precision miniature parts. Prec. Eng., 1(4): 189-198.
7. Gillespie, L.K., 1999. Deburring and Edge Finishing Handbook. SME, Michigan.
8. Jeong, Y. H., HanYoo, B., Lee, H.U., Min, B. K., Cho, D.W., and Lee, S.J., 2009. Deburring microfeatures using micro-EDM. J. Mater. Process. Technol., 209(14): 5399-5406.
9. Dornfeld, D., and Min, S., 2010. A review of burr formation in machining. In Burrs-Analysis, Control and Removal (pp. 3-11). Springer-Verlag, Berlin, Heidelberg.
10. Deburring in Micromachining, http://www.mmsonline.com/blog/post/deburring-in-micromachining (last accessed: June 28 2021).
11. Lee, E.S., Won, J.K., Shin, T.H. and Kim, S.H., 2012. Investigation of machining characteristics for electrochemical micro-deburring of the AZ31 lightweight magnesium alloy. International Journal of Precision Engineering and Manufacturing, 13(3): 339-345.
12. Lee, S.H., 2000. Analysis of precision deburring using a laser - an experimental study and FEM simulation. KSME Int. J., 14(2) : 141-151.
13. Lee, S.H., Dornfeld, D.A., 2001. Precision laser deburring. Journal of Manufacturing Science and Engineering 123(2): 601-608.
14. Zhou, Y., Gao, Y., Wu, B., Tao, S., and Liu, Z., 2014. Deburring effect of plasma produced by nanosecond laser ablation. ASME Journal of Manufacturing Science and Engineering, 136(2): 024501
15. Tao, S., Zhou, Y., Wu, B., and Gao, Y., 2012. Infrared long nanosecond laser pulse ablation of silicon: integrated two-dimensional modeling and time-resolved experimental study. Applied Surface Science, 258(19): 7766–7773
16. Zhou, Y., Tao, S., and Wu, B., 2011. Backward growth of plasma induced by long nanosecond laser pulse ablation. Applied Physics Letters, 99(5): 051106
17. Gusarov, A.V., and Smurov, I., 2005. Thermal model of nanosecond pulsed laser ablation: Analysis of energy mass transfer. J. Appl. Phys., 97: 014307.
18. Jeong, S.H., Greif, R., and Russo, R.E., 1997. Laser heating of metal targets including the influence of the background pressure. Proc. of the ASME Heat Transf. Division, 351: 63-73.
19. Incropera, F.P., Dewitt, D.P., Bergman, T., and Lavine, A.S., 2007. Fundamentals of Heat and Mass Transfer. Wiley, Hoboken, NJ.

20. Gusarov, A.V., Gnedovets, A.G., and Smurov, I., 2000. Gas dynamics of laser ablation: Influence of ambient atmosphere. J. Appl. Phys., 88: 4352-4364.
21. Gurlui, S., Agop, M., Nica, P., Ziskind, M., and Focsa, C., 2008. Experimental and theoretical investigations of a laser-produced aluminum plasma. Phys. Rev. E., 78: 026405.
22. Tannehill, J.C., Anderson, D.A., and Pletcher, R.H., 1997. Computational Fluid Mechanics and Heat Transfer, second ed., Taylor and Francis, Washington, DC.
23. Wu, B., and Shin, Y.C., 2006. Modeling of nanosecond laser ablation with vapor plasma formation. J. Appl. Phys., 99: 084310.
24. Knight, C.J., 1982. Transient vaporization from a surface into vacuum. AIAA J., 20: 950-954.
25. Knight, C.J., 1979. Theoretical modeling of rapid surface vaporization with back pressure. AIAA J., 17: 519-523.
26. Anisimov, S.I., 1968. Vaporization of metal absorbing laser radiation. Sov. Phys. JETP, 27: 182-183.
27. Peterlongo, A., Miotello, A., Kelly, R., 1994. Laser-pulse sputtering of aluminum: Vaporization, boiling, superheating, and gas-dynamic effects. Phys. Rev. E., 50: 4716-4727.
28. Zel'dovich, Y.B., and Raizer, Y.P., 1966-1967. Physics of Shock Waves and High-temperature Hydrodynamic Phenomena. Academic Press, New York and London.
29. Zaghloul, M.R., Bourham, M.A. and Doster, J.M., 2000. A simple formulation and solution strategy of the Saha equation for ideal and nonideal plasmas. Journal of Physics D: Applied Physics, 33(8): 977-984.
30. Kadoya, K., Matsunaga, N. and Nagashima, A., 1985. Viscosity and thermal conductivity of dry air in the gaseous phase. Journal of Physical and Chemical Reference Data, 14(4): 947-970.
31. Mitchner, M., and Kruger, C.H., 1973. Partially Ionized Gases, Wiley, New York.
32. Spitzer, L., 1956. Physics of Fully Ionized Gases, Interscience Publishers, Inc., New York.
33. Liu, X.D., and Osher, S., 1998. Convex ENO high order multi-dimensional schemes without field by field decomposition or staggered grids. J. Comput. Phys., 141: 1 – 27.
34. Chan, C. L., and Mazumder, J., 1987. One-dimensional steady-state model for damage by vaporization and liquid expulsion due to laser-material interaction. Journal of Applied Physics, 62(11): 4579-4586.
35. Boyer, Rodney Welsch, Gerhard Collings, E.W., 1994. Materials Properties Handbook - Titanium Alloys. ASM International. Retrieved from https://app.knovel.com/hotlink/toc/id:kpMPHTA002/materials-properties/materials-properties
36. Johnson, P. B., and Christy, R. W., 1974. Optical constants of transition metals: Ti, V, Cr, Mn, Fe, Co, Ni, and Pd. Physical Review B, 9(12): 5056.
37. David R. Lide (ed), CRC Handbook of Chemistry and Physics. CRC Press. Boca Raton, Florida, 2005; Section 10, Atomic, Molecular, and Optical Physics; Ionization Potentials of Atoms and Atomic Ions.

38. Pedrotti, F.L., Pedrotti, L.S., and Pedrotti, L.M., 2007. Introduction to Optics. Pearson Prentice Hall.
39. Zhou, Y., Wu, B. and Forsman, A., 2010. Time-resolved observation of the plasma induced by laser metal ablation in air at atmospheric pressure. Journal of Applied Physics, 108(9): 093504.
40. Bedford, A., and Liechti, K.M., 2020. Mechanics of Materials, Springer Nature Switzerland AG.
41. Mouritz, A.P. (editor), 2012. Introduction to Aerospace Materials, Woodhead Publishing Limited
42. http://www.knowledgedoor.com/2/elements_handbook/critical_point.html (last accessed on June 29, 2021).

Table 1: Some major titanium properties used in the model [34-37]

Parameter	Value	Unit
Melting point [34]	1940	K
Boiling point [34]	3558	K
Latent heat of fusion (melting) [34]	3.65×10^5	J/kg
Latent heat of vaporization [34]	8.89×10^6	J/kg
Solid density [34]	4500	kg/m^3
Liquid density [34]	4110	kg/m^3
Solid specific heat capacity [34]	528	$J/kg \cdot K$
Liquid specific heat capacity [34]	700	$J/kg \cdot K$
Solid thermal conductivity [34]	21.6	$W/m \cdot K$
Liquid thermal conductivity [34]	20.28	$W/m \cdot K$
Heat capacity ratio of titanium vapor	1.667	-
Atomic weight [35]	47.88	g/mole
Real part of the complex index of refraction for solid titanium at 1064 nm, n_r, [36]	3.47	-
Imaginary part of the complex index of refraction for solid titanium at 1064 nm, n_i, [36]	4.00	-
Ionization potentials	From Ref.[37]	

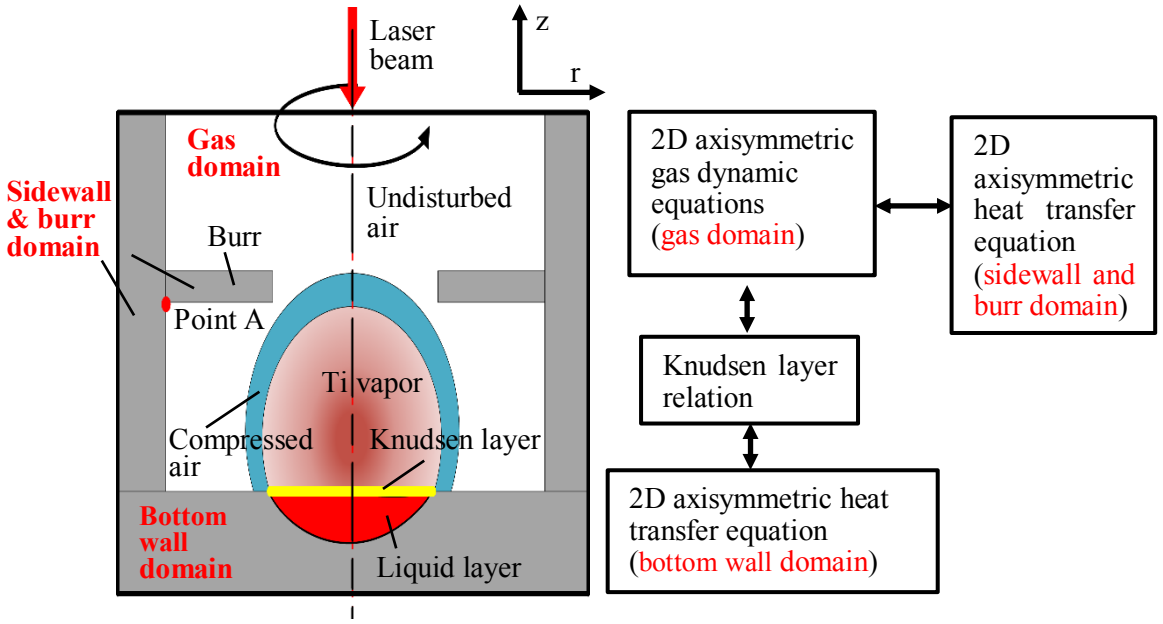

Figure 1. Schematic of the model setup showing the multiple domains involved and the corresponding major governing equations (schematics in this paper may or may not include all the relevant components or illustrate them in an exact way).

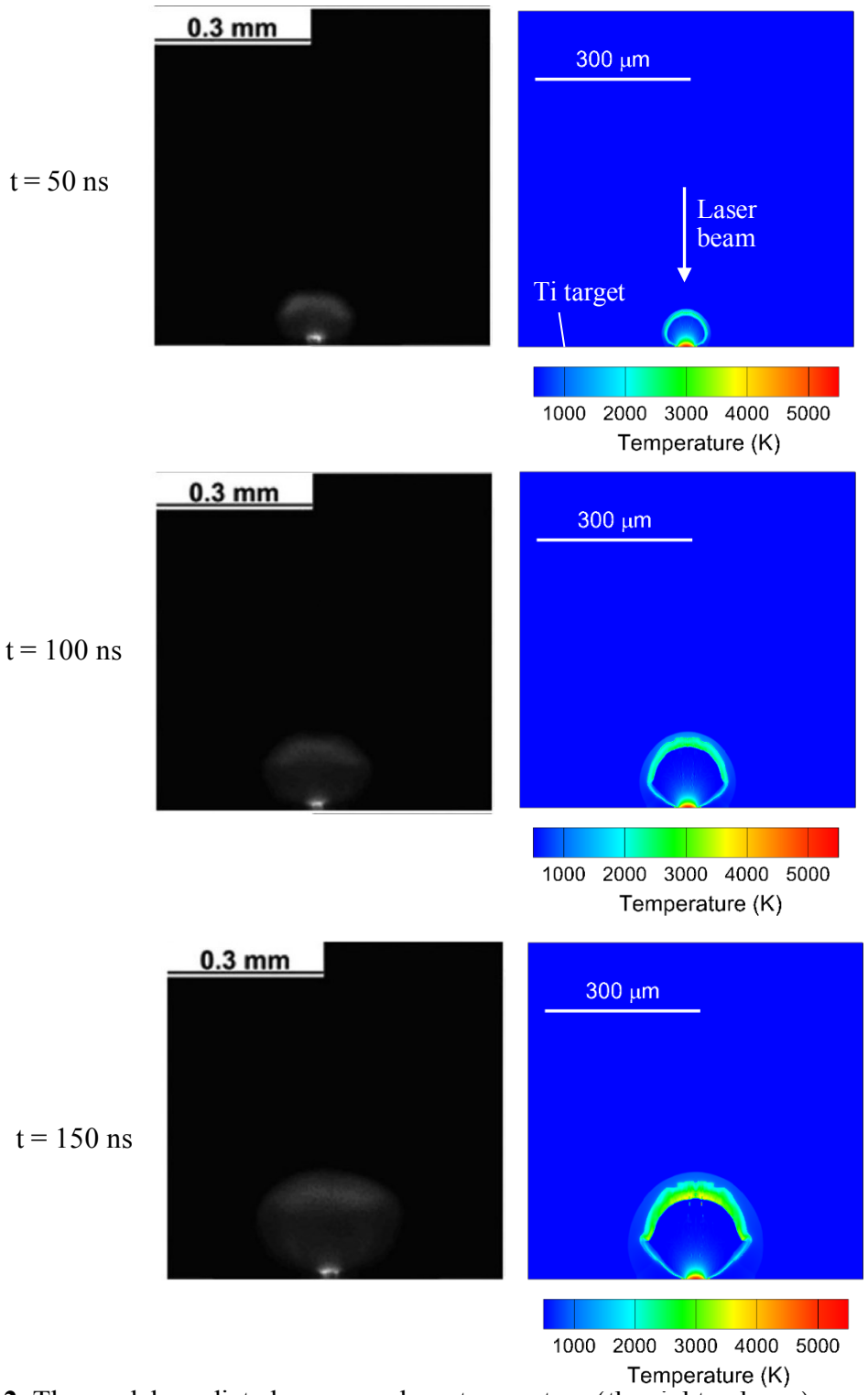

Figure 2. The model-predicted gaseous phase tempeature (the right column) versus the ICCD images (the left column) for plasma plume induced by nanosecond laser pulse ablation of a flat titanium target without any sidewall confiement (laser full pulse duration: ~200 ns, laser pulse starting time: t = 0, wavelength: ~1064 nm, spot diameter: ~30 μm, pulse fluence: ~30 J/cm^2. The ICCD images are taken from the corresponding author's previous paper [39]. That is, the ICCD images are Reprinted from: Zhou, Y., Wu, B. and Forsman, A., 2010. Time-resolved observation of the plasma induced by laser metal ablation in air at atmospheric pressure. Journal of Applied Physics, 108(9): 093504., with the permission of AIP Publishing).

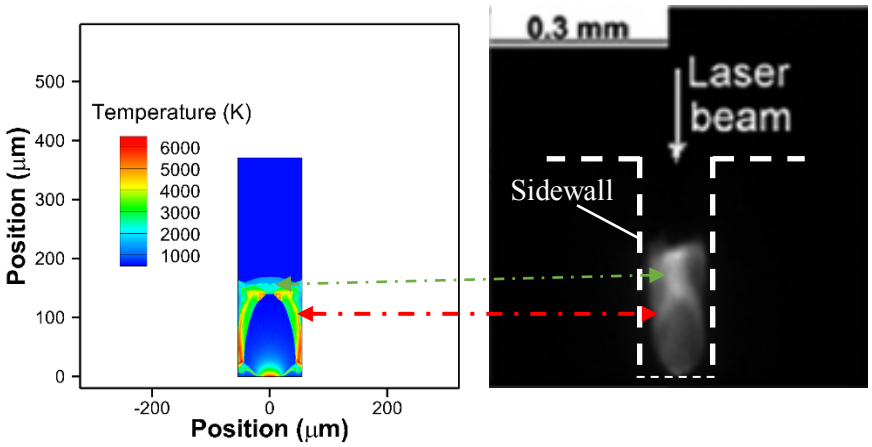

Figure 3. The image of laser ablation-induced plasma plume captured by an ICCD camera (b) versus the gaseous phase temperature predicted by the model (a) at t = 100 ns (the ICCD image is taken from the corresponding author's previous paper [14] with permission. The channel sidewall and bottom wall location is approximately labeled by the dashed line in the ICCD image. Laser full pulse duration: ~200 ns, wavelength: ~1064 nm, pulse energy: ~0.4 mJ, and spot diameter near the channel bottom: ~30 μm. The red arrow indicates that the model-predicted high temperature regions near the sidewall are reasonably consistent with the two bright streaks in a similar location in the ICCD image, which should be formed due to the sidewall confinement effect on the plasma lateral expansion).

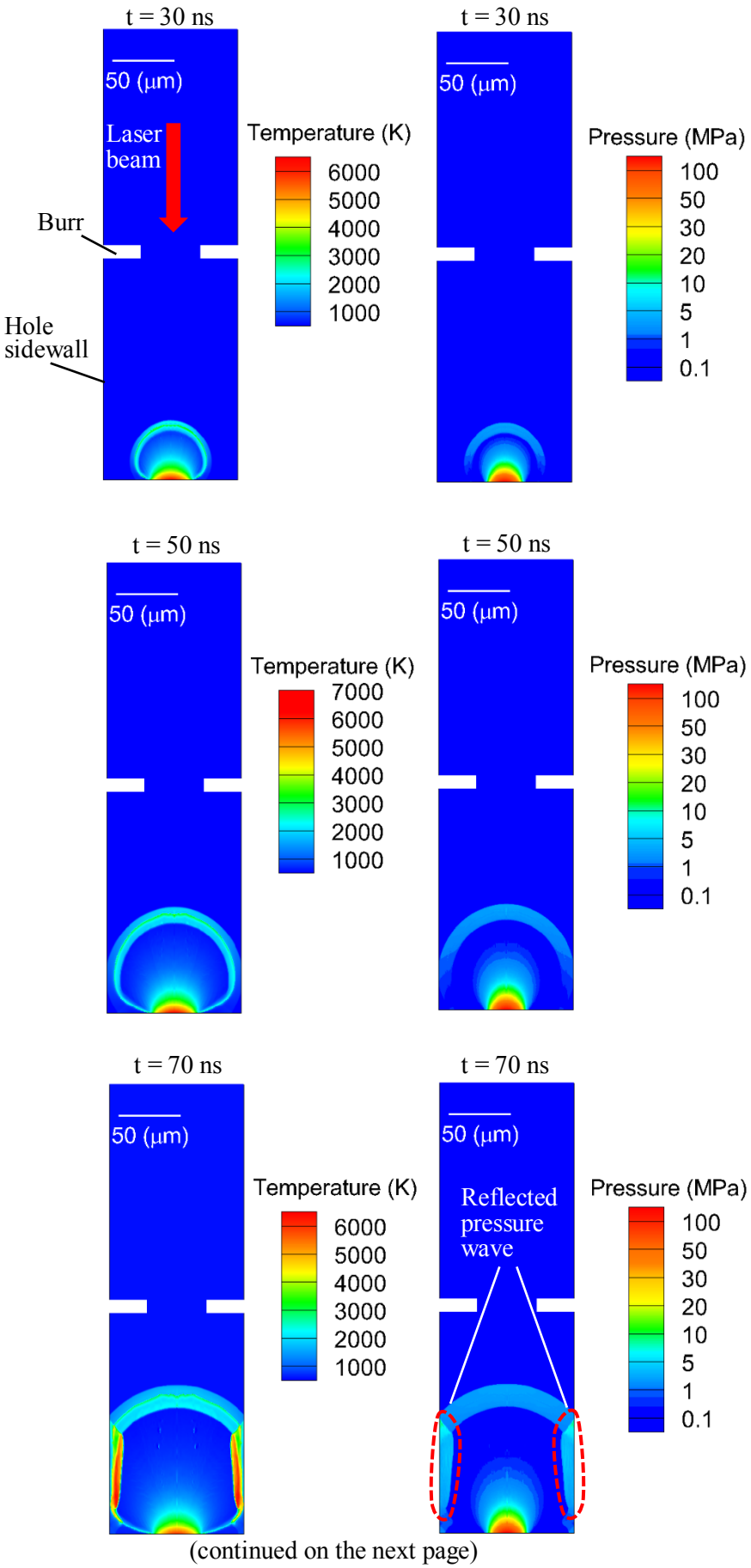

(continued on the next page)

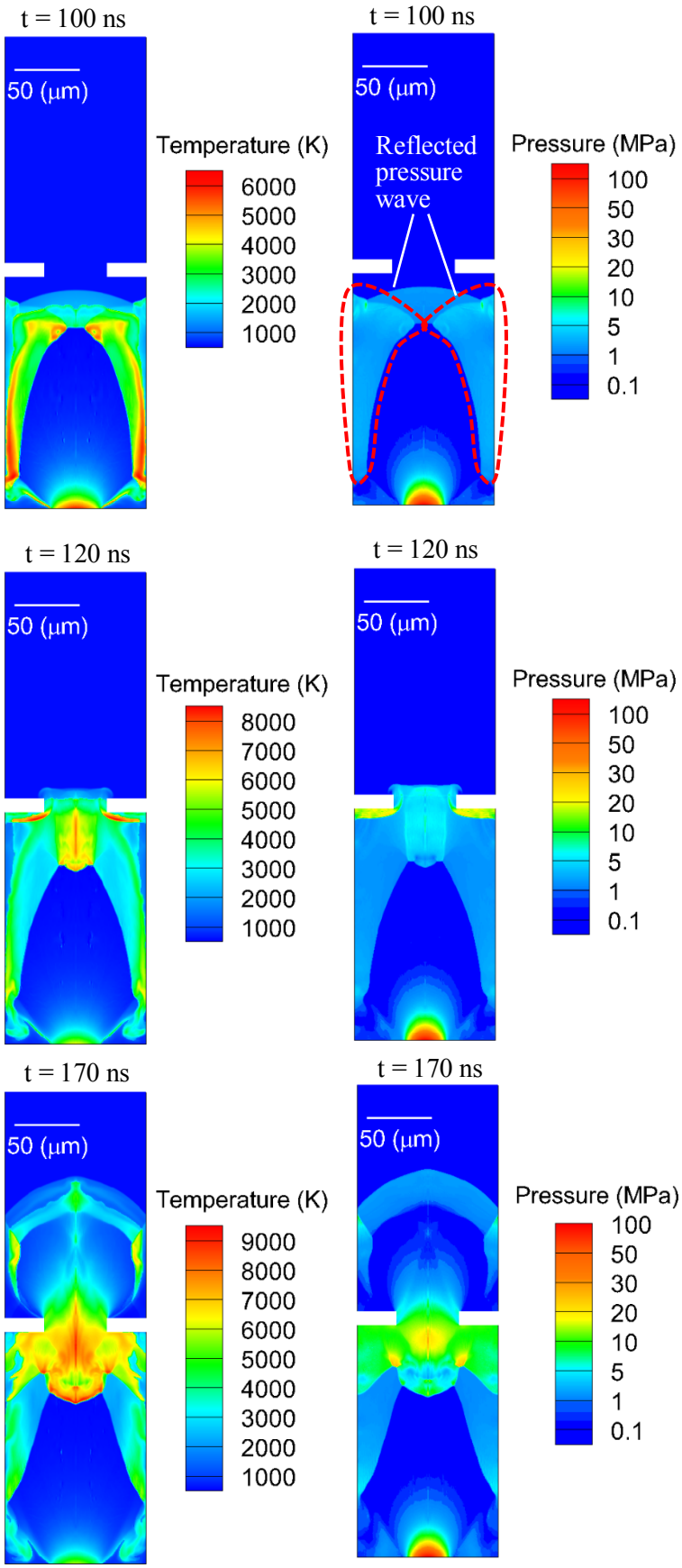

Figure 4. The model-predicted temperature and pressure contour plots at different moments for the gaseous phase for the plasma evolution in a microhole induced by laser pulse ablation of the hole bottom (a 30 × 10 μm burr is located on the hole sidewall and the burr center is 185 μm above the hole bottom; the laser parameters are the same as those for Fig.3).

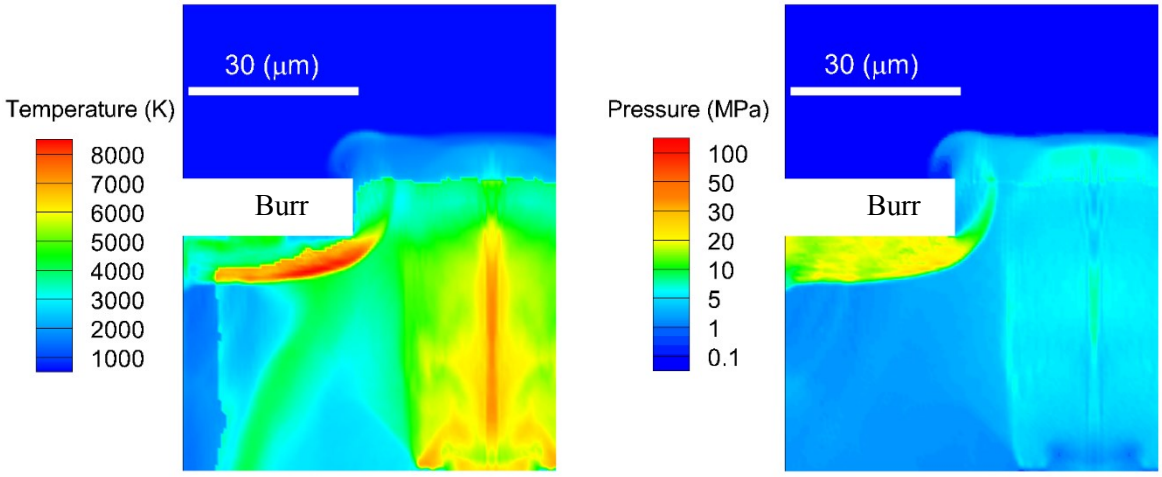

Figure 5. The temperature and pressure contour plots at t = 120 ns for the gaseous phases in the region near the burr for the same simulated case as that in Fig.4.

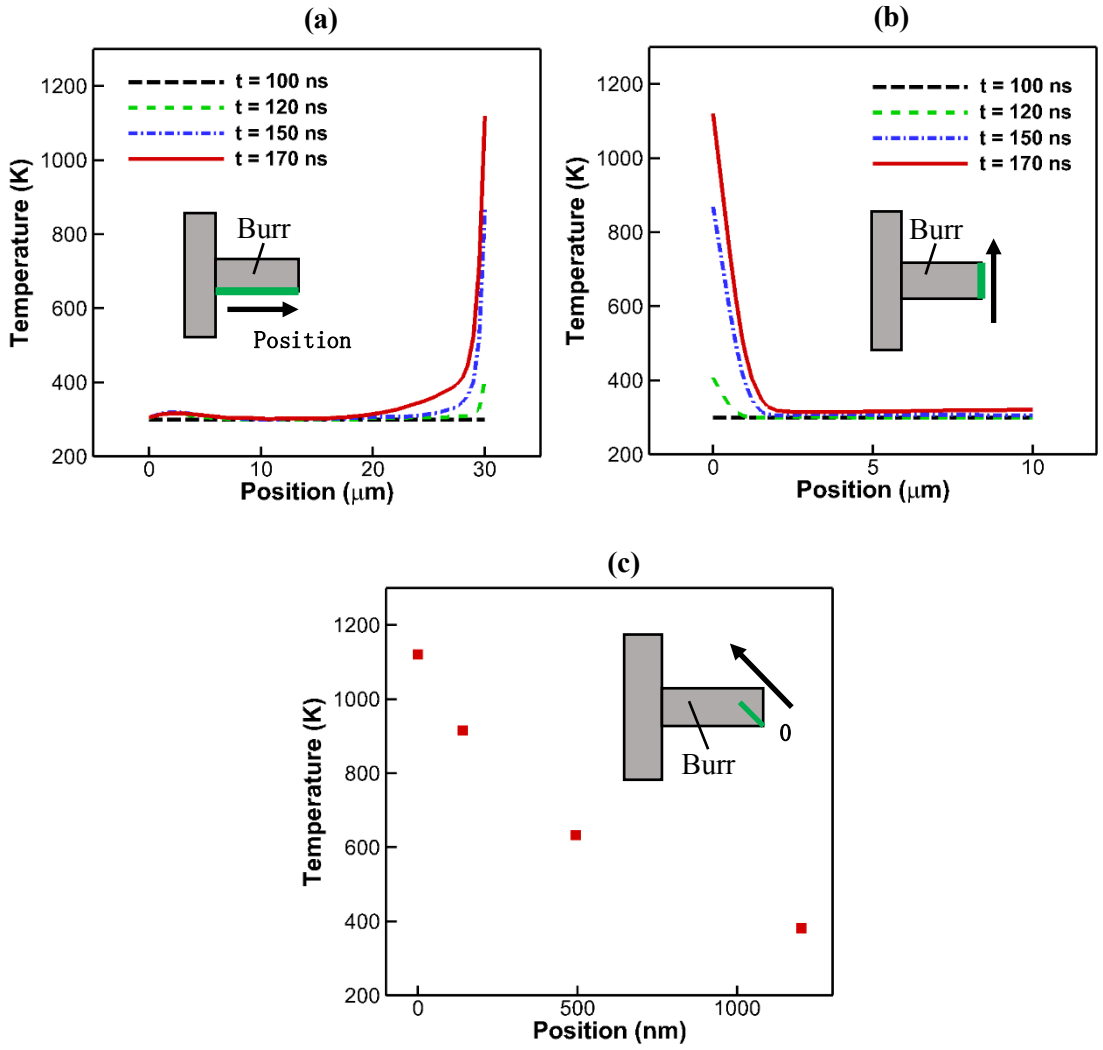

Figure 6. (a) the temperature distributions along the burr bottom surface as indicated by the green line in the inserted schematic at different moments; (b) the temperature distributions along the burr side surface at different moments; (c) the temperature distribution at t = 170 ns along the oblique direction as indicated by the green line in the schematic inserted (45° relative to the horizontal direction) (the results are from the same simulated case as that in Fig.4).

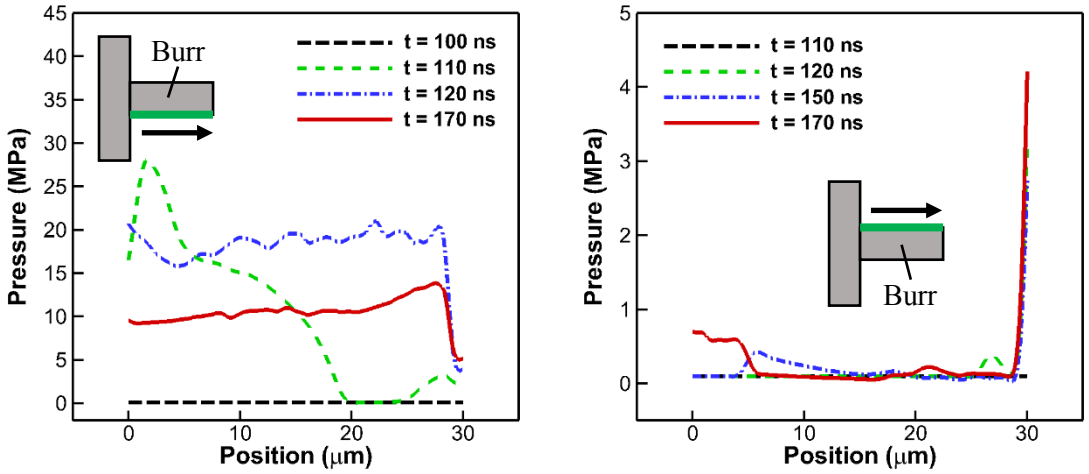

Figure 7. The pressure distributions along the burr bottom surface (a) and the burr top surface (b) at different moments for the same simulated case as that in Fig.4.

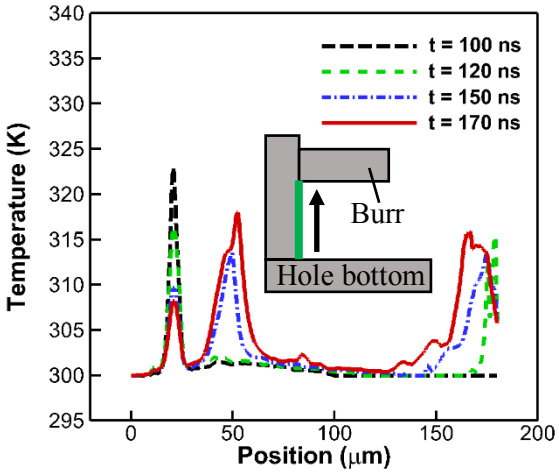

Figure 8. The temperature distributions along the microhole sidewall surface as indicated by the green line in the inserted schematic for the same simulated case as that in Fig.4.

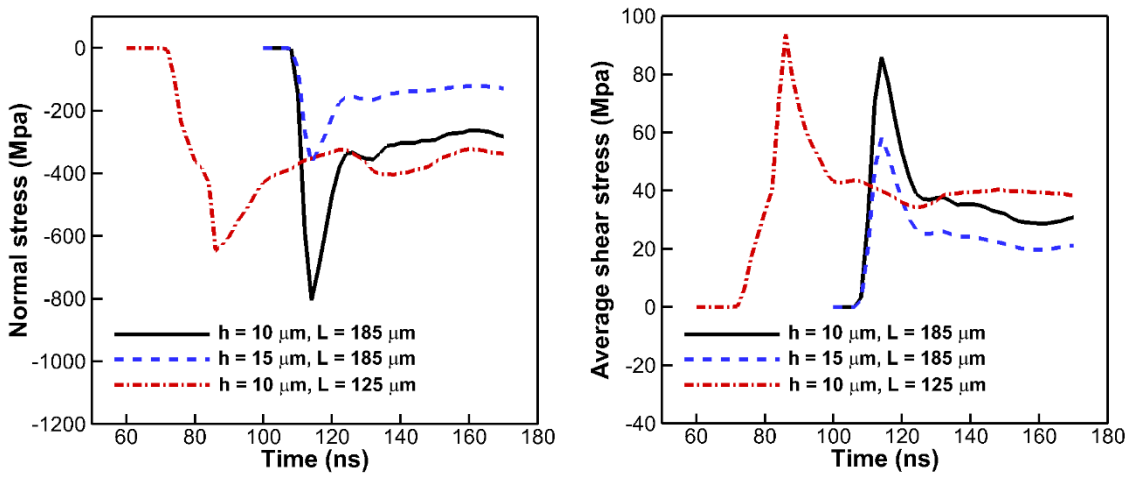

Figure 9. The estimated normal stress for Point A (as defined in Fig.1) (a) and the estimated average shear stress for the burr-sidewall connection plane (b) induced by plasma for 30-μm long burrs with different thicknesses (h) and/or center distances (L) from the channel bottom (for (a), a negative sign is used for tensile normal stresses).